

Using DNA to Design Plasmonic Metamaterials with Tunable Optical Properties

Kaylie L. Young, Michael B. Ross, Martin G. Blaber, Matthew Rycenga, Matthew R. Jones, Chuan Zhang, Andrew J. Senesi, Byeongdu Lee, George C. Schatz,* and Chad A. Mirkin*

Due to their potential for creating ‘designer materials,’ the 3D assembly of nanoparticle building blocks into macroscopic structures with well-defined order and symmetry remains one of the most important challenges in materials science.^[1–5] Furthermore, superlattices consisting of noble-metal nanoparticles have emerged as a new platform for the bottom-up design of plasmonic metamaterials.^[6–8] The allure of optical metamaterials is that they provide a means for altering the temporal and spatial propagation of electromagnetic fields, resulting in materials that exhibit many properties that do not exist in nature.^[9–13] With the vast array of nanostructures now synthetically realizable, computational methods play a crucial role in identifying the assemblies that exhibit the most exciting properties.^[14] Once target assemblies are identified, the synthesis of nanometer-scale structures for use at optical and IR wavelengths must be taken into account. Many of the current methods to fabricate metamaterials in the optical range use serial lithographic-based approaches.^[6] The challenge of controlled assembly into well-defined architectures has kept bottom-up methods that rely on the self-organization of colloidal metal nanoparticles from being fully explored for metamaterial applications.^[8] DNA-mediated assembly of nanoparticles has the potential to help overcome this challenge. The predictability and programmability of DNA makes it a powerful tool for the rational assembly of plasmonic nanoparticles with tunable nearest-neighbor distances and symmetries.^[1,15–18]

Herein, we combine theory and experiment to study a new class of plasmonic superlattices—first using electrostatics simulations to identify that superlattices of spherical silver nanoparticles (Ag NPs) have the potential to exhibit emergent metamaterial properties, including epsilon-near-zero (ENZ) behavior,^[13] and a region with an ‘optically metallic’ response.

Optically metallic materials are DC insulators that reflect in the visible spectrum. This behavior can be described as the opposite of the common touch-screen material, indium tin oxide (ITO), which is transparent in the visible spectrum, but conducts electricity. We then synthesize the first examples of silver nanoparticle superlattices using DNA-mediated assembly and characterize their optical properties with both ensemble measurements and measurements of individual superlattices using spectroscopy. Furthermore, we expand beyond monometallic nanoparticle superlattices to create novel binary superlattices of gold and silver nanoparticle building blocks and observe a Fano-like interference between the two components, leading to a significant dampening of the plasmonic response.

ENZ materials^[19] are a new class of metamaterials that allow for the tunneling of light through a barrier and present the opportunity for arbitrary phase manipulation of light.^[13,20–22] With the global progression of optical fibers and the potential of optical computing, materials will be needed to precisely transmit, modulate, and convert signals on the nanometer scale.^[23,24] Metamaterials consisting of nanoscale noble-metal particles can be engineered to guide and confine light via their tunable localized surface plasmon resonance (LSPR), which is the coherent oscillation of conduction electrons.^[25,26] For many plasmonic applications, silver is preferred to gold due to its sharper LSPR resonances and its ability to span the entire visible spectrum.^[27,28] Several methods for assembling plasmonic nanoparticles into a variety of ordered 3D structures exist, including using the helical nature of DNA to orient nanospheres chirally,^[29] creating liquid-phase-ordered crystal metamaterials,^[30,31] and drying-based methods to create densely packed thin films.^[32] In the context of optical metamaterials, the benefit of using DNA as a programmable linker is that it provides a precise method for varying the size, spacing, and symmetry of inorganic nanoparticles in 3D space.^[18,33,34] Coupled with accurate electrostatics simulations, the dielectric response and collective optical properties of nanoparticle superlattices can be predicted a priori.^[7,25] With a clear understanding of structure–property relationships, we will have the ability to construct optical ‘designer materials,’ i.e., materials that exhibit a set of predetermined properties.

The optical properties of Au NP superlattices have been modeled using Maxwell–Garnett effective medium theory (EMT) in the past.^[35] However, these superlattices were not shown to exhibit negative (real part) dielectric function properties needed for metamaterial behavior. Because Ag NPs are more polarizable than equivalently sized Au NPs,^[28] electrostatics simulations were performed on Ag NP superlattices. For rapid simulation and bulk metamaterial characterization, EMT was used to

Dr. K. L. Young,^[†] M. B. Ross,^[†] Dr. M. G. Blaber,
Dr. M. Rycenga, Dr. C. Zhang, Dr. A. J. Senesi,
Prof. G. C. Schatz, Prof. C. A. Mirkin
Department of Chemistry and
International Institute for Nanotechnology
Northwestern University
2145 Sheridan Road, Evanston, IL 60208, USA
E-mail: schatz@chem.northwestern.edu; chadnano@northwestern.edu
M. R. Jones, Prof. C. A. Mirkin
Department of Materials Science and Engineering
2220 Campus Drive, Evanston, IL 60208, USA
B. Lee
X-ray Science Division
Argonne National Laboratory
9700 South Cass Avenue, Argonne, IL 60439



^[†]These authors contributed equally to this work.

DOI: 10.1002/adma.201302938

generate effective metamaterial parameters for superlattices with varying lattice constants. A modified version of the coupled-dipole method (CDM; see Supporting Information (SI) for full details)^[36–42] was used to visualize the electric field propagation through a superlattice to gain physical insight into the scattering phenomena of Ag NP superlattices.

The simulations were performed on a superlattice consisting of spherical Ag NPs (20 nm in diameter), with well-defined interparticle spacings, which were randomly generated to mimic Au NP superlattices that have been synthesized previously (Figure 1a). Within the framework of EMT, an aggregate consisting of metal nanospheres is described as a homogenous medium (Figure 1b) whose optical constants are defined by the relative concentrations of the constituent materials. The effective dielectric function (ϵ_{eff}) for the Ag NP superlattice is given by:

$$\frac{\epsilon_{\text{eff}} - \epsilon_s}{\epsilon_{\text{eff}} + 2\epsilon_s} = f \frac{\epsilon - \epsilon_s}{\epsilon + 2\epsilon_s} \quad (1)$$

where f is the volume fraction of Ag in the superlattice ($f = V_{\text{metal}}/V_{\text{lattice}}$, Figure 1c), ϵ_s is the dielectric constant of the

solvent (1.77 for water), and ϵ is the complex dielectric function of the metal adjusted for surface scattering.^[41,42] The validity of EMT depends on the strength of the interparticle coupling in a system, and for spheres of 20 nm diameter, it remains valid until approximately 20% (see SI for details). As seen in Figure 1d, ϵ_{eff} is a complex function, where the imaginary part (Im; upper panel) corresponds to the LSPR of the individual nanospheres, and the real part (Re; center panel) describes the nature of the material response (positive for transparent materials, negative for metallic ones). Below this, the extinction (Q_{ext} ; solid line) and the absorption (Q_{abs} ; dashed line) are plotted (bottom panel) for correlation with the electric field plots. Note that although the maximum in Im(ϵ_{eff}) generally correlates with the absorption maximum, this is only true within the quasi-static (small-particle) limit. Because our superlattice has dimensions on the order of a micrometer, the absorption maximum does not align with the Im(ϵ_{eff}) maximum.

A 20% Ag volume fraction superlattice (orange curve, Figure 1d) behaves optically like a metal between 350 and 410 nm, and like a lossy dielectric for wavelengths below approximately 600 nm. Above 600 nm, the superlattice appears as a transparent dielectric with a refractive index of approximately 2. Increasing the fill fraction of metal in the superlattice (by decreasing interparticle spacing; red curve, Figure 1d) increases the imaginary part of the effective dielectric function, which in turn increases the depth of the negative well in the real part to the blue of the LSPR, and also increases the positive peak in the real part (to the red of the LSPR).

ϵ_{eff} can also be used to predict the behavior of the scattered field. Seen in Figure 1d, the real portion of ϵ_{eff} has two highlighted regions, where $\epsilon < 0$ and where $\epsilon \approx 0$. To predict the emergent optical properties of Ag NP superlattices, CDM simulations were performed on the structure depicted in Figure 1a ($f = 20\%$). Below ~350 nm, the response of the simulated material is purely dielectric ($\text{Re}(\epsilon_{\text{eff}}) > 0$; see SI for a plot of the electric field). At about 365 nm ($\text{Re}(\epsilon_{\text{eff}}) \approx 0$, Figure 1e), ENZ behavior is seen in the superlattice.^[13,21] Here, attenuation of the incident field is seen at the boundary of the superlattice. Additionally, some fraction of the incident field is immediately reflected due to the significant boundary mismatch of the refractive index between the superlattice (near zero) and the host media (1.4). At 415 nm, where $\text{Re}(\epsilon_{\text{eff}}) < 0$, we see a slightly altered effect from the ENZ fields. A material with $\text{Re}(\epsilon_{\text{eff}}) < 0$ acts 'optically metallic', showing a finite skin depth, after which the field is attenuated (Figure 1f). Thus, a superlattice consisting of ~20% Ag, and thus ~80% water or dielectric, would appear optically glossy like a metal, yet it would be non-conductive, like a dielectric. For comparison, the

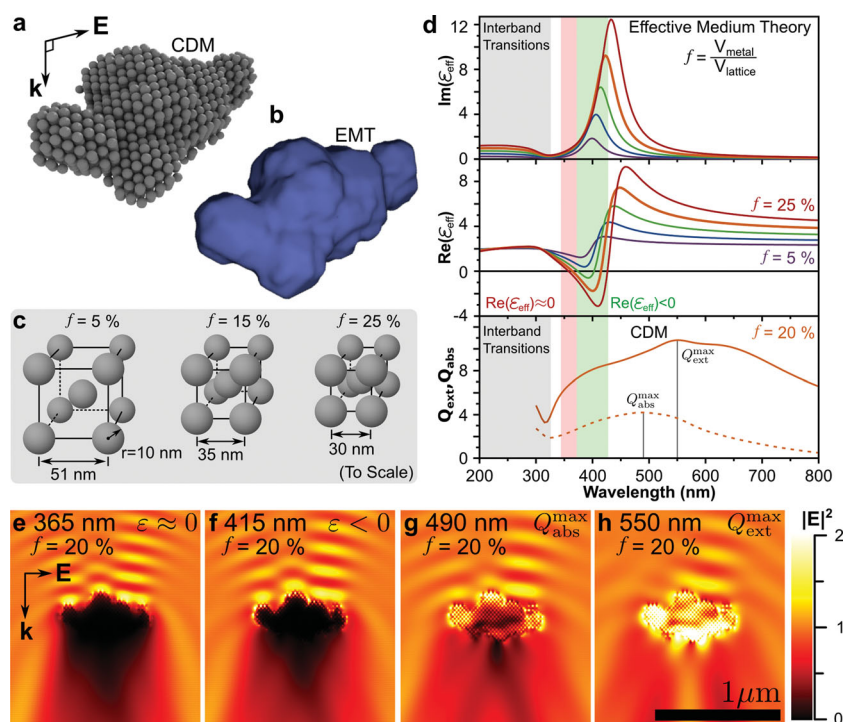


Figure 1. Theoretical scheme for epsilon-near-zero (ENZ) and optically metallic materials. a) Randomly generated superlattice of Ag NPs, showing the incident wave propagation (\mathbf{k}) and polarization (\mathbf{E}) vectors. b) Scheme showing the structure as simulated in effective medium theory (EMT): the internal detail of the superlattice is replaced with a continuous material with a dielectric function described by Maxwell–Garnett EMT. c) A representation of the relationship between lattice constant and fill fraction, showing the proximity of the nanospheres in the lattice; it has been drawn to scale. d) Imaginary (upper panel) and real (center panel) parts of the dielectric function of an Ag NP superlattice with fill fraction, f , varying between 5% and 25%. The lower panel shows the absorption (dashed line) and extinction (solid line) efficiency of the structure in (a), calculated using the CDM. e) Incident electromagnetic field at 365 nm, demonstrating ENZ-material behavior. f) Incident electromagnetic fields at 415 nm indicative of metallic behavior, as seen in the finite penetration depth of the electric field. g) Incident electromagnetic field at the absorption maximum, 490 nm. h) Incident electromagnetic field at the extinction maximum, 550 nm. All simulations were performed with the CDM in a refractive index of 1.4.

electric fields at wavelengths associated with the absorption and extinction maxima (Figure 1d, lower panel) for this superlattice are shown in Figure 1g and h. Notably, the strength of the electric field on the interior of the superlattice is more intense for the absorption and extinction maxima compared to the fields in Figure 1e and f. Forward scattering contributes significantly to the extinction maximum (550 nm), and thus the incident field is focused in the direction of propagation (Figure 1h).

Having demonstrated that Ag superlattices with volume fractions between 15% and 25% should demonstrate either ENZ or optically metallic behavior that is tunable with the lattice constant, we utilized DNA-programmable methods to experimentally synthesize such structures. Ag NPs are more challenging to incorporate experimentally than gold nanoparticles (Au NPs) due to the chemical degradation of the Ag NPs under DNA functionalization conditions and their susceptibility to surface oxidation.^[27] However, our group recently developed a method for functionalizing Ag NPs with a dense layer of oligonucleotides,^[43] which are analogous to the Au-NP-based spherical nucleic acids (SNAs).^[44] In this work, Ag NPs with diameters of ~20 and ~30 nm were functionalized with DNA oligonucleotides containing three terminal cyclic disulfide (DSP) groups to serve as a robust anchor. DNA linkers with single-stranded “sticky ends” that facilitate hybridization between NPs were added in a predetermined ratio, and the samples were annealed slightly below their melting temperature to form crystalline aggregates (Figure 2a). Importantly, these Ag NP aggregates displayed sharp melting transitions (see SI for melting analysis) indicative of co-operative binding, a requirement for the synthesis of well-ordered nanoparticle superlattices.^[33,45]

The Ag NPs functionalized with a dense layer of DNA oligonucleotides were then used to synthesize one-component face-centered cubic (FCC) and two-component body-centered cubic (BCC) crystal structures using linkers that were self-complementary (5'-GCGC-3') and non-self-complementary (5'-TTCTT-3' and 5'-AAGGA-3'), respectively (Figure 2).^[15,18] Superlattices with more complex unit cells were also synthesized (see SI). As we have previously demonstrated, the most stable crystal structure is that which maximizes the number of DNA hybridization events between neighboring nanoparticles.^[18] The 3D crystalline structures of the superlattices were characterized by in-situ synchrotron small-angle X-ray scattering (SAXS), and the data were compared to the scattering patterns of the analogous atomic lattices for position and intensity of the allowed reflections. The large number of sharp diffraction peaks that are observed for the FCC and BCC Ag NP superlattices (Figure 2b,e) are indicative of highly ordered crystals with domain sizes on the micrometer-scale. In a complementary method, the Ag NP superlattices were embedded in a polymer resin, sectioned, and characterized by scanning transmission electron microscopy (STEM) to obtain a “snapshot” of the crystals that exist in solution (Figure 2c,d,f). It is important to note that the embedding process results in a reduction of the interparticle spacing, but maintains the crystallographic symmetry calculated from the SAXS pattern. In order to measure the optical properties of individual Ag NP superlattices without modifying their symmetry or lattice spacing, the Ag NP superlattices were stabilized in the solid state using a silica encapsulation method (see SI for details).^[47]

The nearest-neighbor spacing, and therefore lattice parameters, of the FCC and BCC crystals can be

tuned with nanometer precision by changing the number of DNA bases in the linkers.^[48] For the Ag NP superlattices, each nucleobase adds 0.244 nm. In this work, the length of the linkers was tuned using modular blocks of 40 bases, denoted by parentheses in Figure 2a, allowing us to probe the effects of interparticle plasmonic coupling in an extended periodic 3D structure. Each integer increment of n corresponds to an increase of ~9.7 nm on each NP, or ~19.5 nm total between neighboring NPs. Using 20 nm Ag NPs, BCC superlattices were assembled and characterized with interparticle distances of 31.7 ± 0.6 nm ($n = 0$), 52.8 ± 0.8 nm ($n = 1$), and 71.8 ± 1.2 nm ($n = 2$) (standard deviation determined from four separate batches of superlattices), corresponding to surface-to-surface distances between neighboring Ag NPs of approximately 12, 32, and 52 nm, respectively. The SAXS pattern for each of the three systems confirms high-quality crystals with BCC symmetry (Figure 2g).

The collective optical properties of the superlattices were then analyzed experimentally, using both UV-vis spectroscopy for ensemble measurements and optical microspectrophotometry for individual superlattice

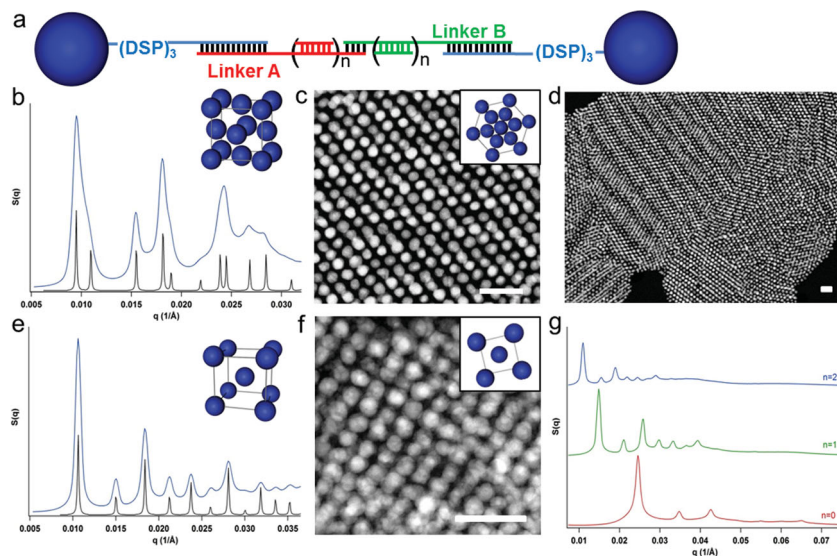


Figure 2. Characterization of FCC and BCC superlattices assembled from Ag NPs. a) Schematic illustration of DNA-programmable nanoparticle crystallization where the length of the linker strands can be tuned by increasing the value of n . DSP refers to cyclic dithiol. b) SAXS pattern and corresponding unit cell and c,d) STEM images of an FCC lattice synthesized from 30 nm Ag NPs. The zoomed-out image (d) shows multiple crystalline domains within a superlattice. e) SAXS pattern and corresponding unit cell and f) STEM image of a BCC lattice synthesized from 20 nm Ag NPs. Experimental data are shown in blue and predicted scattering patterns are shown in black. All scale bars are 100 nm. g) SAXS patterns of 20 nm Ag NP superlattices with BCC symmetry with tunable interparticle spacings (red: 31.7 nm ($n = 0$), green: 52.8 nm ($n = 1$), blue: 71.8 nm ($n = 2$)).

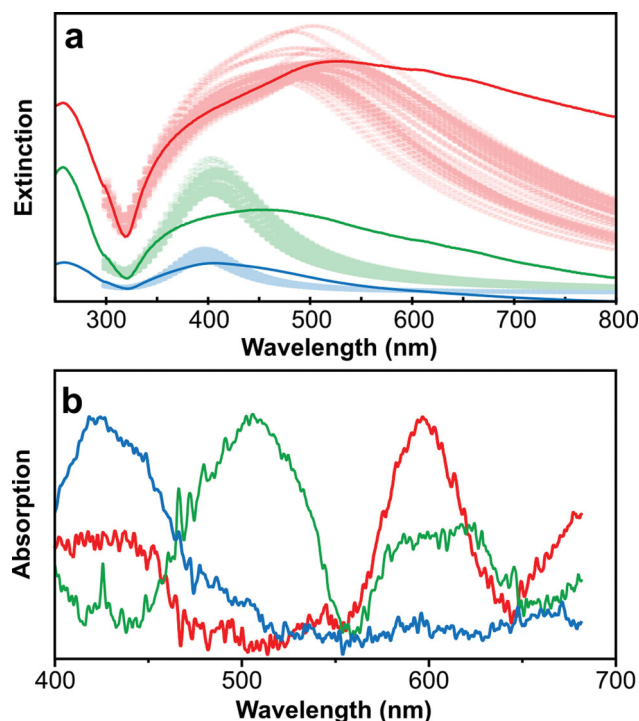


Figure 3. Optical characterization of Ag NP superlattices (experimental data and simulations). a) UV-vis spectra taken in water of as-synthesized Ag NP BCC superlattices with varying interparticle spacings, and thus, metal fill fractions (solid traces; red: $n = 0$, 17.1% Ag; green: $n = 1$, 3.7% Ag; blue: $n = 2$, 1.5% Ag). Simulated spectra of randomly generated orientationally averaged superlattices in a refractive index of 1.4 are underlaid with corresponding colors, albeit a lighter shade. b) Single superlattice measurements of absorption spectra taken with a micro-spectrophotometer. Spectra were chosen that are representative of the statistical data (see SI for tabulated data). Note the difference in the scales of the x-axes.

measurements. Using UV-vis spectroscopy (Figure 3a), red-shifting of the superlattices' bulk LSPR with decreased nanoparticle spacing is observed. This can be explained primarily by the increase in Ag fill fraction (i.e., an increase in dipole-dipole interactions, provided that they are weak) with decreased interparticle spacing.^[49] Additionally, electrodynamics simulations were performed using the CDM. For correlation with the UV-vis ensemble measurements, superlattices with varying shape, but with well-defined interparticle spacing, were randomly generated to best mimic the superlattices observed with STEM (see SI for construction method). CDM simulations on these structures are in good agreement with the experimental UV-vis extinction spectra (Figure 3a). It is difficult, however, to determine rigorous structure-property relationships with ensemble measurements. The inherent averaging and solution-based nature of UV-vis spectroscopy makes it difficult to separate the effects of nanoparticle spacing and superlattice size.^[50] Thus, individual superlattices were analyzed using a micro-spectrophotometer (see SI for details).^[51,52]

After depositing silica-embedded Ag nanoparticle superlattices on a Formvar grid, STEM was used to select superlattices with sizes between 700 and 800 nm. Because the Formvar and silica encapsulation affect scattering, and therefore extinction

measurements, absorption spectra were determined from transmission and reflection measurements (see SI for method). Thus, the plasmonic response of the Ag NP superlattices with varying interparticle spacings was determined with bright-field measurements using the micro-spectrophotometer. Figure 3b shows that ' $n = 0$ ' superlattices demonstrate the most red-shifted absorption, with an average maximum absorption, λ_{max} , of 594 nm. With increased spacing, the absorption is blue-shifted (Figure 3b), with average λ_{max} values of 530 nm ($n = 1$) and 448 nm ($n = 2$). We note that these measurements are consistent both between superlattices from a single sample and between different batches of superlattices, with standard deviations in λ_{max} of less than 4% for all spacings (see SI for tabulated data). The red-shift seen between the micro-spectrophotometer measurements (Figure 3b) and the UV-vis ensemble measurements (Figure 3a) is attributed to the silica-embedding process, which changes the local refractive index and the interaction between the superlattice and the Cu Formvar TEM grid. Additionally, non-uniformities in the superlattice aggregates can lead to the formation of additional lines in the individual superlattice measurements. For example, in the green trace of Figure 3b, an extra peak can be observed at ~600 nm. This is likely due to asymmetry in the superlattice shape; the complex structure of the aggregates can result in multiple plasmon resonances from different parts of the aggregate (see, for example, Figure 1). In addition, it is possible that the distance between the superlattice and the Formvar is not uniform across the entire structure, resulting in changes to the structure of the LSPR spectrum. The low variation in absorption maxima from different superlattices (tabulated in SI) suggests that the absorption of similarly sized superlattices is consistent. From this, we conclude that the primary reason that the LSPR red-shifts with decreased interparticle spacing is due to the increase in Ag fill fraction.^[35]

Once the emergent optical properties of DNA-mediated Ag NP superlattices were investigated, we introduced DNA-functionalized Au NP building blocks to allow for the assembly of binary (Ag NP)-(Au NP) superlattices. Although there have been some examples of DNA-programmable heterogeneous nanoparticle assemblies in 3D space to date,^[53–56] the functional properties of these materials have yet to be explored. To synthesize the binary Ag-Au superlattices, a two-component system with non-self-complementary linkers, similar to those used to create the Ag NP BCC crystals, was utilized. The two components consisted of Ag NPs (20 or 30 nm diameter) functionalized with DSP-terminated DNA oligonucleotides and Au NPs (15, 20, or 30 nm diameter) functionalized with monothiol-terminated DNA oligonucleotides (Figure 4a). The simplest binary system, in which the Ag and Au NPs are identical in size, and added in a 1:1 ratio, results in an AB-type crystal (isostructural with CsCl), characterized by SAXS and STEM (Figure 4b,c). As shown in Figure 4b, the experimental SAXS pattern is in strong agreement with the calculated diffraction pattern, confirming the long-range order of the system. Crystal structures with increasingly complex unit cells can be synthesized with a two-component system by tuning the hydrodynamic radii and linker ratios of each component according to the design rules that have been established for DNA-mediated Au NP crystallization.^[18] Binary (Ag NP)-(Au NP) superlattices of the

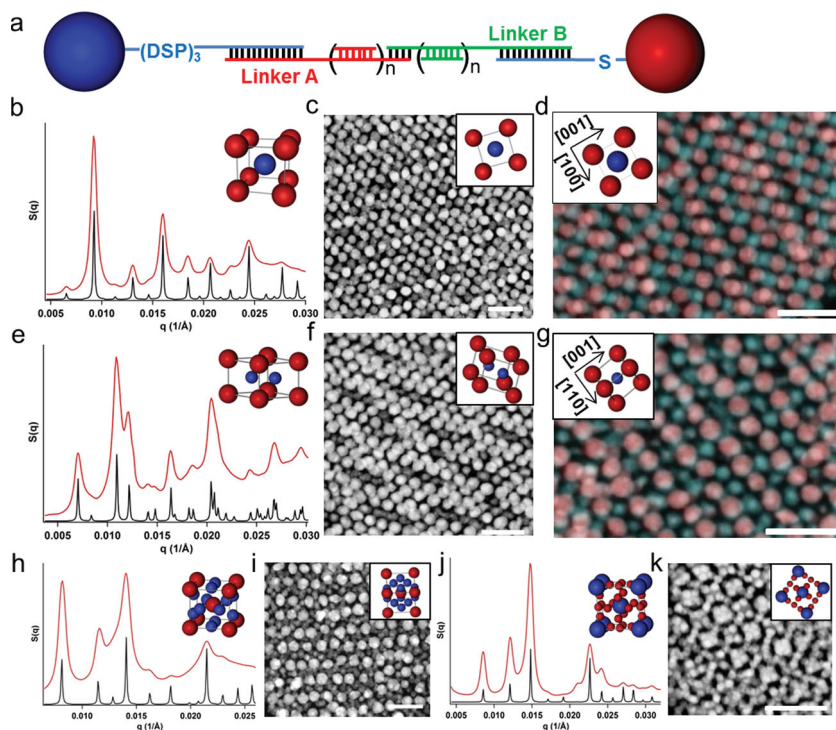


Figure 4. Characterization of binary superlattices assembled from Ag and Au NPs. a) Schematic illustration of the assembly of binary Ag–Au NP superlattices where the linker lengths can be tuned by increasing n . b, c, e, f, h–k) SAXS patterns (and the corresponding unit cell) and STEM images of binary Ag–Au NP superlattices that are isostructural with CsCl (b, c), AlB₂ (e, f), Cr₃Si (h, i), and Cs₆C₆₀ (j, k). In the SAXS patterns, experimental data are shown in red and predicted scattering patterns are shown in black. The insets of the STEM images show the unit cell viewed along the appropriate projection axis. d, g) EDX elemental maps of AB- (d) and AB₂-type (g) binary lattices with the zone axis shown in the insets. Gold signal is shown in red and silver signal is shown in blue. All scale bars are 100 nm.

AB₂-type (isostructural with AlB₂) with a hexagonal unit cell (cell parameter c/a ratio = 0.73) were synthesized using 30 nm Au NPs with the ' $n = 2$ ' linker at the corners of the unit cell and 20 nm Ag NPs with the ' $n = 1$ ' linker in the middle (Figure 4e, f). Importantly, an AB₂-type crystal can also be achieved by swapping the components, i.e., using 30 nm Ag NPs with the ' $n = 2$ ' linker and 20 nm Au NP building blocks with the ' $n = 1$ ' linker; thus demonstrating the versatility of the DNA-mediated approach to assembly (see SI). By varying the radii and linker ratios of the Ag and Au components, binary AB₃-type (isostructural with Cr₃Si) and AB₆-type (isostructural with Cs₆C₆₀) superlattices were also synthesized (Figure 4h–k). All binary superlattices were confirmed with SAXS and imaged by electron microscopy (Figure 4).

Although the Ag NPs have lower contrast than Au NPs in the STEM images of the binary Ag–Au NP crystals, the identity of the NPs can be determined using energy-dispersive X-ray (EDX) elemental mapping. When EDX maps of Au and Ag are overlaid on the corresponding STEM image (Figure 4d, g), the zone axis becomes immediately obvious. Thus, in addition to potential emergent collective properties, the incorporation of Ag into DNA-mediated superlattices provides an elemental handle to unequivocally confirm the symmetry of the unit cell that is determined using SAXS.

Interestingly, when solution-phase ensemble UV–vis measurements were collected for the 3D binary CsCl-type (Ag NP)–(Au NP) superlattices, the peak at 410 nm (corresponding to the LSPR of the Ag NPs) was significantly dampened when compared to a solution of dispersed Ag and Au NPs in an equal ratio (Figure 5a). Furthermore, the dampening is more pronounced as the interparticle distance was decreased through the use of shorter DNA linkers. This observation was further investigated by simulating the system using generalized multiparticle Mie (GMM) theory (Figure 5b).^[57–59] At the closest nearest-neighbor surface-to-surface distance of ~10 nm ($n = 0$), the LSPR peaks of Ag and Au are equivalent in intensity and significantly broadened. This is surprising because Ag NPs have a much higher extinction coefficient than Au NPs of the same diameter.^[27] To understand the interaction between the Ag and Au NPs in the extended lattice structure, the per-particle optical absorption and scattering cross-sections were plotted for each material separately (Figure 5c, d). As is shown in Figure 5c, there is a Fano-like^[26] dip in the absorption efficiency of Au at 370 nm when the surface-to-surface distance is 10 nm. Additionally, a greater decrease is seen in the Ag absorption per-particle relative to the Ag scattering per particle (Figure 5d). Recently, plasmonic coupling has been investigated between Au and Ag NP dimers^[60,61] and in 2D arrays of plasmonic nanoparticles made lithographically^[62] or chemically and separated by nonplasmonic NPs.^[32] Theoretical studies by Bachelier et al. have predicted the presence of a Fano profile in dimers of Ag NPs and Au NPs due to coupling of the LSPR of the Ag NP with the Au interband transitions.^[60] The experimental observation of this Fano profile is challenging due to the orientational averaging that occurs in solution-phase measurements^[63] and the need to isolate the absorption cross-sections of the Ag and Au separately.^[61] In the binary Ag–Au colloidal crystals, the LSPR of the Ag NPs serves as the discrete level and the gold interband transitions serve as the continuum. Thus the dampening of the Ag LSPR in the binary (Ag NP)–(Au NP) superlattices, observed experimentally and in GMM simulations, is due to a Fano-like interference between the resonant silver mode and the interband transitions of gold.

In conclusion, electrodynamics simulations were used to identify that superlattices of Ag NPs have the potential to exhibit unusual metamaterial behavior, including ENZ behavior and an 'optically metallic' region that exhibits high reflectivity despite the fact that the superlattices are over 80% water. DNA was used as a programmable linker to assemble spherical silver nanoparticles into 3D periodic assemblies, and the optical response of the Ag NP superlattices was shown to be heavily dependent on the interparticle spacing (and hence the metal fill fraction) within the superlattices. DNA-programmable assembly allows

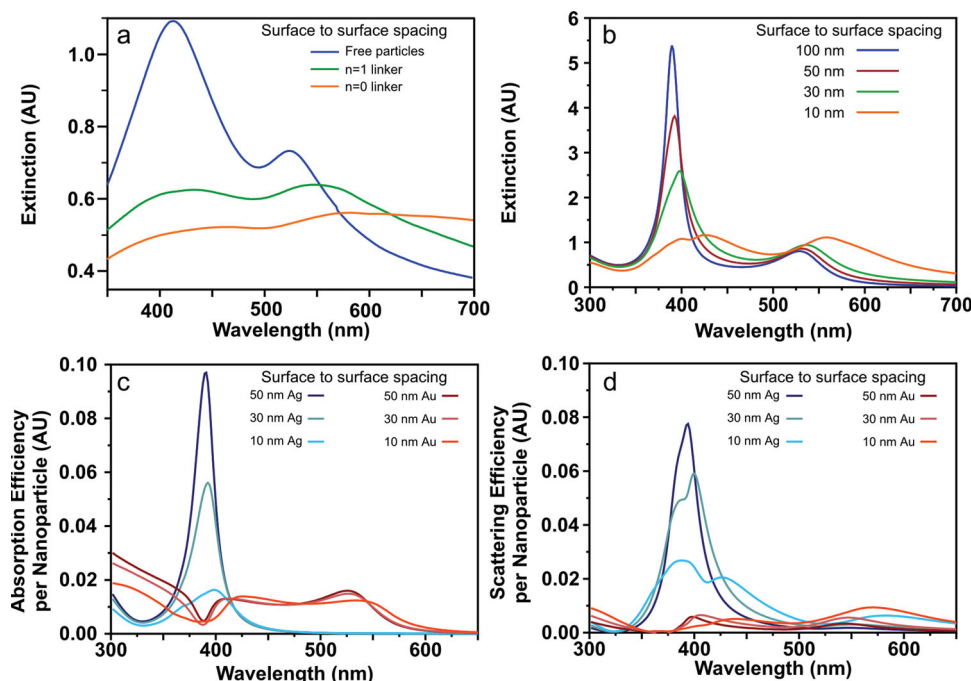


Figure 5. Optical characterization and simulations of AB-type Ag–Au binary superlattices. a) Experimental data: UV–vis spectra of unassembled, DNA-functionalized Ag and Au nanoparticles (blue), Ag–Au superlattices with $n = 1$ linker (green), and Ag–Au superlattices with $n = 0$ linker (orange). b) Simulated data: extinction of Ag–Au superlattices at various surface-to-surface distances. c) Simulated absorption efficiency per nanoparticle of Ag–Au binary superlattices at various surface-to-surface distances. d) Simulated scattering efficiency per nanoparticle of Ag–Au binary superlattices at various surface-to-surface distances. All simulations performed with generalized multiparticle Mie theory.

for the precise control of NP spacing, making it attractive for the study of structure–property relationships and the construction of designer materials. The experiments detailed herein represent one of the first studies of the functional properties of colloidal superlattices engineered with DNA. The use of DNA as a programmable assembly tool in conjunction with electrodynamics simulations can be used for the effective design of plasmonic metamaterials with potential for use in the creation of optical circuitry and interconnects,^[10,23,24] optical cloaking materials,^[9,21] and data exchange.^[13,20]

MRSEC award DMR-1121262. G.C.S. also acknowledges support from NSF/MRSEC award DMR-0520513. K.L.Y. and M.B.R. gratefully acknowledge support through NDSEG graduate fellowships. K.L.Y. and M.R.J. gratefully acknowledge support from the NSF through the Graduate Research Fellowship Program (GRFP). Use of the Advanced Photon Source was supported by the Office of Basic Energy Sciences, US DOE under Contract DE-AC02-06CH11357. Electron microscopy was carried out in the Electron Probe Instrumentation Center facility of the Northwestern University Atomic and Nanoscale Characterization Experimental Center.

Received: June 28, 2013

Revised: August 28, 2013

Published online: October 25, 2013

Experimental Section

See detailed description of experimental materials and methods and simulations in the SI.

Supporting Information

Supporting Information is available from the Wiley Online Library or from the author.

Acknowledgements

C.A.M. and G.C.S. acknowledge support from AFOSR MURI Award FA9550-11-1-0275 and the Department of Energy Office (DOE Award DE-SC0000989) through the Northwestern University Nonequilibrium Energy Research Center. C.A.M. also acknowledges support from AFOSR Awards FA9550-09-1-0294 and FA9550-12-1-0280 and NSF/

- [1] C. A. Mirkin, R. L. Letsinger, R. C. Mucic, J. J. Storhoff, *Nature* **1996**, 382, 607.
- [2] R. J. Macfarlane, M. N. O'Brien, S. H. Petrosko, C. A. Mirkin, *Angew. Chem. Int. Ed.* **2013**, 52, 5688.
- [3] Z. Nie, A. Petukhova, E. Kumacheva, *Nat. Nanotechnol.* **2010**, 5, 15.
- [4] A. Travesset, *Science* **2011**, 334, 183.
- [5] S. Gwo, M.-H. Lin, C.-L. He, H.-Y. Chen, T. Teranishi, *Langmuir* **2012**, 28, 8902.
- [6] K. J. Stebe, E. Lewandowski, M. Ghosh, *Science* **2009**, 325, 159.
- [7] H. Alaeian, J. A. Dionne, *Opt. Express* **2012**, 20, 15781.
- [8] A. R. Tao, D. P. Ceperley, P. Sinsermsuksakul, A. R. Neureuther, P. Yang, *Nano Lett.* **2008**, 8, 4033.
- [9] D. R. Smith, J. B. Pendry, M. C. K. Wiltshire, *Science* **2004**, 305, 788.
- [10] A. Alu, N. Engheta, *Opt. Express* **2007**, 15, 7578.
- [11] P. Y. Chen, J. Soric, A. Alu, *Adv. Mater.* **2012**, 24, Op281.

- [12] M. Silveirinha, N. Engheta, *Phys. Rev. Lett.* **2006**, 97, 157403.
- [13] N. Engheta, *Science* **2013**, 340, 286.
- [14] M. J. Solomon, *Curr. Opin. Colloid Interface Sci.* **2011**, 16, 158.
- [15] S. Y. Park, A. K. R. Lytton-Jean, B. Lee, S. Weigand, G. C. Schatz, C. A. Mirkin, *Nature* **2008**, 451, 553.
- [16] D. Nykypanchuk, M. M. Maye, D. van der Lelie, O. Gang, *Nature* **2008**, 451, 549.
- [17] S. J. Tan, M. J. Campolongo, D. Luo, W. Cheng, *Nat. Nanotechnol.* **2011**, 6, 268.
- [18] R. J. Macfarlane, B. Lee, M. R. Jones, N. Harris, G. C. Schatz, C. A. Mirkin, *Science* **2011**, 334, 204.
- [19] E. J. R. Vesseur, T. Coenen, H. Caglayan, N. Engheta, A. Polman, *Phys. Rev. Lett.* **2013**, 110, 013902.
- [20] A. Alu, M. G. Silveirinha, A. Salandrino, N. Engheta, *Phys. Rev. B* **2007**, 75.
- [21] A. Alu, N. Engheta, *Opt. Express* **2007**, 15, 3318.
- [22] A. Alu, N. Engheta, *J. Appl. Phys.* **2006**, 99.
- [23] H. A. Atwater, *Sci. Am.* **2007**, 296, 56.
- [24] N. Engheta, *Science* **2007**, 317, 1698.
- [25] K. L. Kelly, E. Coronado, L. L. Zhao, G. C. Schatz, *J. Phys. Chem. B* **2003**, 107, 668.
- [26] N. J. Halas, S. Lal, W. S. Chang, S. Link, P. Nordlander, *Chem. Rev.* **2011**, 111, 3913.
- [27] M. Rycenga, C. M. Cobley, J. Zeng, W. Li, C. H. Moran, Q. Zhang, D. Qin, Y. Xia, *Chem. Rev.* **2011**, 111, 3669.
- [28] M. G. Blaber, M. D. Arnold, M. J. Ford, *J. Phys.: Condens. Matter* **2010**, 22, 143201.
- [29] A. Kuzyk, R. Schreiber, Z. Fan, G. Pardatscher, E.-M. Roller, A. Hoge, F. C. Simmel, A. O. Govorov, T. Liedl, *Nature* **2012**, 483, 311.
- [30] Q. Liu, Y. Cui, D. Gardner, X. Li, S. He, I. I. Smalyukh, *Nano Lett.* **2010**, 10, 1347.
- [31] Q. Liu, B. Senyuk, J. Tang, T. Lee, J. Qian, S. He, I. I. Smalyukh, *Phys. Rev. Lett.* **2012**, 109, 088301.
- [32] X. Ye, J. Chen, B. T. Diroll, C. B. Murray, *Nano Lett.* **2013**, 13, 1291.
- [33] R. J. Macfarlane, M. R. Jones, A. J. Senesi, K. L. Young, B. Lee, J. Wu, C. A. Mirkin, *Angew. Chem.* **2010**, 122, 4693.
- [34] R. J. Macfarlane, M. R. Jones, B. Lee, E. Auyeung, C. A. Mirkin, *Science* **2013**, 341, 1222.
- [35] A. A. Lazarides, K. Lance Kelly, T. R. Jensen, G. C. Schatz, *J. Mol. Struct. Theochem.* **2000**, 529, 59.
- [36] M. J. Collinge, B. T. Draine, *J. Opt. Soc. Am. A* **2004**, 21, 2023.
- [37] B. T. Draine, P. J. Flatau, *J. Opt. Soc. Am. A* **1994**, 11, 1491.
- [38] B. T. Draine, P. J. Flatau, *arXiv:1202.3424 [physics.comp-ph]* **2012**.
- [39] B. T. Draine, J. Goodman, *Astrophys. J.* **1993**, 405, 685.
- [40] P. J. Flatau, B. T. Draine, *Opt. Express* **2012**, 20, 1247.
- [41] P. B. Johnson, R. W. Christy, *Phys. Rev. B* **1972**, 6, 4370.
- [42] U. Kreibig, Vonfrags C. v., *Z. Phys.* **1969**, 224, 307.
- [43] J.-S. Lee, A. K. R. Lytton-Jean, S. J. Hurst, C. A. Mirkin, *Nano Lett.* **2007**, 7, 2112.
- [44] J. I. Cutler, E. Auyeung, C. A. Mirkin, *J. Am. Chem. Soc.* **2012**, 134, 1376.
- [45] H. D. Hill, J. E. Millstone, M. J. Banholzer, C. A. Mirkin, *ACS Nano* **2009**, 3, 418.
- [46] M. R. Jones, R. J. Macfarlane, B. Lee, J. Zhang, K. L. Young, A. J. Senesi, C. A. Mirkin, *Nat. Mater.* **2010**, 9, 913.
- [47] E. Auyeung, R. J. Macfarlane, C. H. J. Choi, J. I. Cutler, C. A. Mirkin, *Adv. Mater.* **2012**, 24, 5181.
- [48] H. D. Hill, R. J. Macfarlane, A. J. Senesi, B. Lee, S. Y. Park, C. A. Mirkin, *Nano Lett.* **2008**, 8, 2341.
- [49] T. Atay, J.-H. Song, A. V. Nurmikko, *Nano Lett.* **2004**, 4, 1627.
- [50] J. J. Storhoff, A. A. Lazarides, R. C. Mucic, C. A. Mirkin, R. L. Letsinger, G. C. Schatz, *J. Am. Chem. Soc.* **2000**, 122, 4640.
- [51] J. J. Mock, M. Barbic, D. R. Smith, D. A. Schultz, S. Schultz, *J. Chem. Phys.* **2002**, 116, 6755.
- [52] L. J. Sherry, S. H. Chang, G. C. Schatz, R. P. Van Duyne, B. J. Wiley, Y. N. Xia, *Nano Lett.* **2005**, 5, 2034.
- [53] C. Zhang, R. J. Macfarlane, K. L. Young, C. H. Choi, L. Hao, E. Auyeung, G. Liu, X. Zhou, C. A. Mirkin, *Nat. Mater.* **2013**, 12, 741.
- [54] E. Auyeung, J. I. Cutler, R. J. Macfarlane, M. R. Jones, J. Wu, G. Liu, K. Zhang, K. D. Osberg, C. A. Mirkin, *Nat. Nanotechnol.* **2012**, 7, 24.
- [55] M. A. Kostianinen, P. Hiekkataipale, A. Laiho, V. Lemieux, J. Seitsonen, J. Ruokolainen, P. Ceci, *Nat. Nanotechnol.* **2013**, 8, 52.
- [56] D. Sun, O. Gang, *J. Am. Chem. Soc.* **2011**, 133, 5252.
- [57] Y.-I. Xu, *Appl. Opt.* **1995**, 34, 4573.
- [58] Y.-I. Xu, *Appl. Opt.* **1997**, 36, 9496.
- [59] Y.-I. Xu, R. T. Wang, *Phys. Rev. E* **1998**, 58, 3931.
- [60] G. Bachelier, I. Russier-Antoine, E. Benichou, C. Jonin, N. Del Fatti, F. Vallée, P. F. Brevet, *Phys. Rev. Lett.* **2008**, 101, 197401.
- [61] S. Sheikholeslami, Y.-w. Jun, P. K. Jain, A. P. Alivisatos, *Nano Lett.* **2010**, 10, 2655.
- [62] C. L. Haynes, A. D. McFarland, L. Zhao, R. P. Van Duyne, G. C. Schatz, L. Gunnarsson, J. Prikulis, B. Kasemo, M. Käll, *J. Phys. Chem. B* **2003**, 107, 7337.
- [63] J. H. Yoon, Y. Zhou, M. G. Blaber, G. C. Schatz, S. Yoon, *J. Phys. Chem. Lett.* **2013**, 4, 1371.